Validation Plan

for

MODIS Level 1 At-Sensor Radiance

Kurtis J. Thome

Remote Sensing Group

of the

Optical Sciences Center

University of Arizona
Tucson, Arizona 85721

April 22, 1999

Table of Contents

1.0 Introduction

This document describes the activities that the Remote Sensing Group (RSG) of the Optical Sciences Center at the University of Arizona will use to evaluate and validate the Level-1 radiance from MODIS. It reviews recent activities related to this effort and describes planned activities for time period up to two years after launch. The methods that are described in this document are often referred to as vicarious calibration (VC) that is defined here as the use of calibrated sources external to the sensor, MODIS in this case, in order to validate the radiances as derived by on-board calibration and preflight methods (Slater et al, 1996).

1.1 Science objectives

MODIS will view the entire surface of the Earth every 1-2 days, making observations in 36 co-registered spectral bands. These data will be collected at moderate spatial resolutions of 250 to 1000 m and processed to provide land and ocean surface temperature, primary productivity, land surface cover, clouds, aerosols, water vapor, temperature profiles, and fires. Critical to this work is understanding the radiometric behavior of the sensor. Registered radiance at sensor is essential for the generation of these higher-level data products and validation of the registered radiance at sensor allows for comparisons of these data with data from other instruments that are part of the Earth Sciences Enterprise (ESE) and other Earth-observation satellites.

1.2 Missions

The first MODIS sensor is part of the EOS Terra platform due for launch in July 1999. A second MODIS sensor will fly onboard EOS PM-1 due to be launched December 2000. The Terra platform will be in a sun-synchronous, near-polar orbit with and Equator crossing time of approximately 10:30 am. The PM-1 platform is planned for a similar orbit with an afternoon crossing time of 13:30 PM. The focus of this document is on the calibration/radiance validation of Terra MODIS. However, the methods described here are directly applicable to PM-1.

1.3 Science data products

The MODIS product covered by this validation plan is the Level-1 radiances.

2.0 Validation Overview

2.1 Objectives

According to the EOS Validation Program, validation is defined as "... the process of assessing by independent means the uncertainties of the data products derived from system outputs." This process can be accomplished either through comparisons with correlative, but independent, measurements (often referred to as ground truth) or through comparisons with other satellite-sensor retrievals. In the case of validating the reported Level-1 radiances by MODIS, the system outputs are the digital numbers (DNs) reported by MODIS and the data product is at-sensor radiance.

While the RSG has typically viewed vicarious calibration as a techniques for calibrating sensors, one can also take the view that these methods can be used to validate the at-satellite radiances. These

at-satellite radiances are either determined from preflight calibrations or from onboard calibrators. The onboard calibrators that MODIS will rely on use several techniques that have yet to be proven for satellite-sensor calibration. Thus, it becomes important for the success of the mission to understand the accuracy of these onboard calibrators. The primary objective of this work is to provide information to the MODIS Calibration Support Team (MCST) to evaluate the transfer-to-orbit of the preflight calibration of the sensor and the operation of the onboard calibrators.

2.2 Overall approach

The overall validation procedure uses the at-sensor radiance from a selected test site measured by MODIS using the most recent set of calibration coefficients. These MODIS-derived radiances are compared to those predicted from the validation data collections. Three ground-reference methods will be used: reflectance-based, irradiance-based, and radiance-based methods. In the VNIR and SWIR, all three approaches are used. In addition, a cross-calibration technique will be used for both the solar reflective and TIR. Cross-calibration uses simultaneously-acquired data from other instruments onboard the Terra platform such as ASTER and MISR or other well-characterized sensors with similar bandpasses on other platforms (such as Landsat-7 Enhanced Thematic Mapper+ (ETM+)).

2.2.1 Reflectance-based method

The reflectance-based approach relies on ground-based surface reflectance measurements of a selected target at the time of sensor overpass (Slater et al., 1987). The surface reflectance of a small area of the site is found by comparing radiometer measurements of the site to those from a diffusely reflecting panel of known reflectance calibrated at RSG facilities using a pressed polytetrafluoroethylene standard. The calibration reference is a directional-to-hemispheric reflectance standard provided by NIST. Polynomial fits are made to the measured data to calculate the reflectance of the field standard for the sun-view geometry and wavelengths for a given set of field measurements (Biggar et al., 1988).

A spectroradiometer, transported across the entire site, measures the upwelling across the spectral range between 350 and 2500 nm. The spectroradiometer collects a number of samples along a straight-line path within some fraction of the area representing a MODIS pixel. Reflectance of the site is determined in each spectral channel by comparing measurements of the site to those of the calibrated panel and averaging all of the measurements. Sun-angle changes and the bi-directional reflectance of the reflectance panel are taken into account when determining the reflectance. Global irradiance data are used to determine the significance of changes in diffuse skylight illumination.

The primary instrument used to characterize the atmosphere over the site is the solar radiometer. The solar radiometers are relatively calibrated immediately prior to, during, or after each field campaign. Data are used in a Langley method retrieval scheme to determine spectral-atmospheric optical depths (Gellman et al., 1991). The optical depth results are used as part of an inversion scheme developed by the RSG to determine ozone optical depth and a Junge aerosol size distribution parameter (Biggar et al., 1990). The size distribution and columnar ozone are used to determine the optical depths at 1-nm intervals from 350 to 2500 nm. Columnar water vapor is derived using a modified Langley approach (Thome et al., 1992). Here, as for the optical depth retrieval, the primary uncertainty in

water vapor is the instrument's relative calibration. The retrieved columnar water vapor is used as an input to MODTRAN3 to determine transmittance for the sun-to-surface-to-satellite path for 1-nm intervals from 350 to 2500 nm. In the thermal infrared, the atmospheric measurements concentrate on obtaining profiles of temperature and humidity using radiosonde balloons.

All of these results are used as input to a Gauss-Seidel iteration radiative transfer code to predict the top-of-the-atmosphere radiance (Herman and Browning, 1965). We compare the average of the digital numbers of the selected site as reported by the sensor to these predicted radiances to give the radiometric calibration.

This method has been used to calibrate small footprint sensors such as TM, SPOT HRV, and multiple airborne sensors. This method is also suitable for the calibration of ETM+ and ASTER. Because of the use of lighter radiometers, it is also now possible to apply the reflectance-based method directly to MODIS.

2.2.2 Irradiance-based method

The reflectance-based approach relies on numerous assumptions about the size and composition of aerosols in the atmosphere. If these assumptions are incorrect, then the computed radiance at the top of the atmosphere can be in error. In order to reduce the problems of some of these assumptions, the irradiance-based approach was developed (Biggar, et al. 1990b). This method uses measurements of the downwelling, global and diffuse irradiances to determine the radiance at the top of the atmosphere according to

$$L_\lambda(0_v,0_s,\Delta\varphi) = \frac{E_{0\lambda}\cos(0_s)}{\pi}\left[\varrho_{A\lambda}(0_v,0_s,\Delta\varphi)+\varrho_\lambda(1-\varrho_\lambda S_\lambda)\left(\frac{e^{-\delta_\lambda/\cos(0_v)}}{1-\alpha_{v\lambda}}\right)\left(\frac{e^{-\delta_\lambda/\cos(0_s)}}{1-\alpha_{s\lambda}}\right)\right] \quad \textbf{(1)}$$

where

$L_\lambda(\theta_v, \theta_s, \Delta\phi)$ is the radiance at the top of the atmosphere for a satellite view angle of θ_v with the sun at a zenith angle of θ_s and the difference in azimuth between the sun and view direction is $\Delta\phi$

$E_{0\lambda}$ is the solar irradiance at the top of the atmosphere for the earth-sun distance at the time the data are acquired

$\rho_{A\lambda}$ is the apparent reflectance that would be measured for the case of a zero-reflectance surface and apparent reflectance is $\pi L_{\lambda A}(\theta_v, \theta_s, \Delta\phi)/E_{0\lambda}$ and $L_{\lambda A}$ is the intrinsic path radiance.

ρ_λ is the surface reflectance

S_λ is the spherical albedo of the atmosphere, that is, the ratio of the downwelling irradiance at the ground for a given set of atmospheric conditions to the reflected irradiance for the same conditions

δ_λ is the vertical, spectral optical thickness

$\alpha_{s\lambda}$ and $\alpha_{v\lambda}$ are the diffuse-to-global-irradiance ratios with the sun at zenith angles θ_s and θ_v respectively.

Of these quantities, ρ_λ, δ_λ, $\alpha_{s\lambda}$ are measured in the field at the time of satellite overpass, $E_{0\lambda}$ is determined from the literature (for example, Iqbal, 1983), θ_s is determined from the time of overpass, and S_λ and $\rho_{A\lambda}$ can be found from radiative transfer calculations based on atmospheric parameters derived using the methods described in the section on the reflectance-based approach. All that remains to compute the radiance at the sensor is to determine $\alpha_{v\lambda}$. In the case where the sun reaches the elevation angle of the satellite sensor, the diffuse-to-global ratio is measured when the sun is at the appropriate elevation and is used in (1). Of course, this assumes that the atmosphere is azimuthally homogeneous and temporally invariant between the time of actual sensor overpass and the time at which the sun is at the sensor elevation. In the case where the sun does not rise high enough in the sky, measurements throughout the morning are extrapolated to the appropriate geometry. This approach also assumes that the composition of the atmosphere does not change with time.

2.2.3 Radiance-based method

In the radiance-based approach, the radiometer measurements of the upwelling energy from the test site are no longer ratioed to measurements of a field-reference panel. Rather, the field radiometer is absolutely calibrated in the laboratory and the upwelling radiance from the test site is determined directly from the measurements. Because no reference-panel measurements are needed, the radiometer can be flown in an aircraft and the radiance can be measured above much of the scattering influences of the atmosphere. An atmospheric correction is still performed using ground-based data and the RTC mentioned earlier, but the correction is quite small. In fact, it is possible to use this method in a fashion similar to Hovis et al. (1985) and make no atmospheric correction. The results of such a method are not as accurate, but the advantage is that more remote sites can be used and a greater number of calibrations can be performed. An additional advantage to flying the radiometer is that a much larger test site can be measured in a short period of time. This approach can thus be applied to the calibration of MODIS.

Of course, the characterization and calibration of the radiometer becomes a critical factor in this method. Currently, we use a 4-band radiometer with 1-degree FOV that gives about a 30-m spot size for typical altitudes of our test sites. This radiometer is not connected to the aircraft power system and measurements are recorded by independent data loggers. The radiometer is either hand pointed from a helicopter or mounted to a fixture viewing through a belly port in a light aircraft. In each case, a video camera, bore sighted with the radiometer, allows accurate determination of which data were collected over the test site. The filters for the radiometer are chosen to match the filters of the sensor to be calibrated and are in regions of the spectrum where silicon detector responsivity is not sensitive to temperature.

Once the sensors have been calibrated, they are flown in an aircraft that allows the measurements to be made above much of the effects of the water vapor and the scattering by aerosols. The radiometers will be flown up to about 3 km above sea level. Based on previous work by the RSG, this altitude is high enough so that the uncertainty due to the atmospheric correction of the radiance at the satellite sensor in the solar reflective range is within +/- 0.1%.

2.2.4 Cross-calibration

The above methods can also be modified for large footprint sensors to become what we term cross-calibration (Teillet et al., 1990, and Teillet et al. 1992). A block diagram of a cross-calibration method is shown in Fig. 2-1. One way to view this method is that a well-characterized, calibrated, satellite sensor is used to determine the surface reflectance of the selected target. This surface reflectance is used in a reflectance-based approach to determine the radiance at the entrance aperture of the uncalibrated sensor.

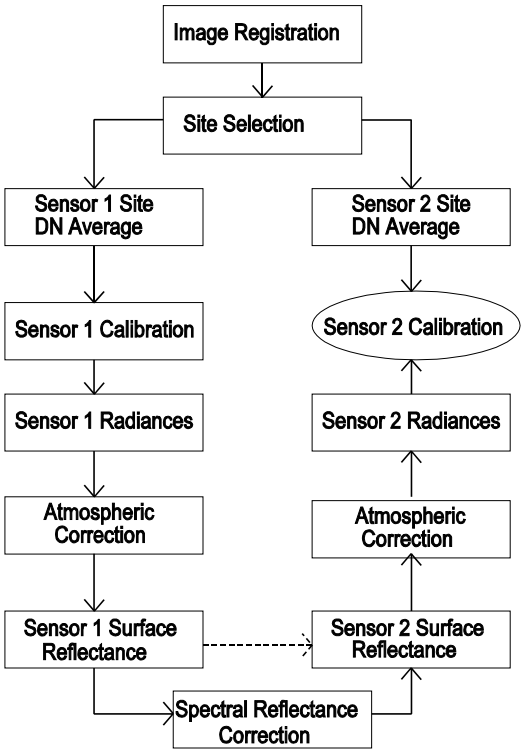

Figure 2-1.. Block diagram of the cross-calibration approach in which Sensor 1 is assumed to be calibrated and Senor 2 uncalibrated.

The first step is to register data from the two sensors. For small-footprint sensors this is done using ground-control points in the two images. Large surface features or boundaries are used for large footprint sensors. Once the images are registered, a calibration site within the images is selected and the average DN of the site for both sensors is found. The DNs for the calibrated sensor (sensor 1 in Figure 2-1) are converted to radiance using the known calibration coefficients and surface reflectance of the target is found using these radiances and an atmospheric correction approach. The correction scheme uses radiative transfer code output to derive a relationship between surface reflectance and at-sensor radiance. This is assumed to be linear over small intervals of reflectance and the surface reflectance is found through linear interpolation.

The reflectance for the site for the bands of sensor 1 are used to determine the surface reflectance of the site for the band of interest of sensor 2. For some targets it is possible to assume spectral differences between sensors are negligible, and the reflectance for sensor 2 is identical to that of sensor 1. Typically, this is not the case, and it is necessary to account for such differences using ground-based data, either current or historical. The ground reflectance may also require a correction for BRF effects at this stage due to different viewing angles and solar-angle changes between overpasses for cases when the two sensors are not on the same platform. The surface reflectance for the bands of sensor 2 are converted to radiance by reversing the atmospheric correction scheme and these radiances are compared to the DNs to determine its calibration coefficient.

Cross-calibration approaches are also suitable for work in the TIR for ASTER, ETM+, and MODIS. This cross-calibration work will allow us to determine if there are any biases between the three

systems. Our intent in the TIR is not to perform an accurate absolute calibration, but rather a precise relative calibration to determine if there are any problems with the onboard blackbodies. For ASTER and MODIS, the largest uncertainties will be from spectral differences in the bands due to spectral emissivity and atmospheric effects. For the cross-calibration of ETM+ we will also have to consider temporal changes in the surface temperature of the test site. Using a large water target such as Lake Tahoe should reduce the emissivity and temporal effects, but much work will have to be done to determine band-to-band effects due to the atmosphere.

2.2.5 Laboratory calibration and NIST traceability

A key element to the above-described methods is to maintain traceability to a national standard of radiance. Since MODIS and other Terra platform sensors built in the United States are maintaining traceability to NIST, this work does the same. This ensures that differences found between the vicarious calibrations and onboard calibrations are not due to biases in the transfer to absolute units.

2.3 Measures of success

The radiance validation of MODIS will be considered a success when the results of this work agree with the radiances derived using MCST-derived calibration coefficients to within the uncertainties of the methods. This will be accomplished by improvement of the precision and accuracy of the vicarious methods such that there is confidence that differences between predicted TOA radiances from the validation are real effects. When significant differences occur, the RSG will work with MCST to determine the cause of the difference.

3.0 Vicarious calibration sites

The most critical part of vicarious calibration is the proper selection of suitable test sites. In this section, we describe the characteristics that reduce the uncertainties in the calibration and then describe four test sites that are in current use by the RSG.

3.1 Desired characteristics

Vicarious calibration requires careful selection of the test site used. Through past work we have identified the most important characteristics an ideal site (Scott, 1996):

1) A relatively bright site reduces the impact of errors in determining the path radiance component during the radiative transfer calculations. A nominal site reflectance greater than 0.3 ensures that the site radiance is the dominant contributor to the TOA radiance.

2) An elevation of at least one kilometer reduces the amount of atmospheric aerosols and the errors associated with predicting their characteristics and concentrations.

3) High spatial uniformity over a large area minimizes the effects of misregistration when performing a cross-calibration. In particular, a uniform area of at least 2 × 2 km in size is desired. This size allows for a one-half pixel misregistration on all sides. The level of uniformity required is more difficult to quantify other than to say "the more uniform the better." By simulating reflectance errors in a radiative transfer code calculation, it becomes clear that reflectance errors induce nominally a one-to-one correspondence in errors in TOA radiance calculations, and the

corresponding gain coefficients (the errors vary some depending on the sensor band and atmospheric conditions). Hence, if a reflectance of 0.55 is assumed instead of 0.5 (a 9% difference), a 9.7% difference is seen in the TOA radiance for typical atmospheric conditions. A goal of 2% uniformity for the desired site keeps this uncertainty to an acceptable level.

4) Minimal seasonal variations are desired if possible as well as a site that is free of vegetation that can affect seasonal variability, as well as BRF characteristics. An arid region is also desired to improve the probability of cloud-free days and to minimize reflectance variations due to ground moisture content.

5) The site should be nearly lambertian to decrease uncertainties due to changing solar and view geometry when cross-calibrating sensors on different platforms. A flat site also has the advantage of reducing BRF effects and eliminating shadow problems.

6) Spectral uniformity of the site is considered important over as wide a region as possible to simplify sensor mismatch corrections. In particular, it is desired that the site have the same reflectance from the VNIR into the SWIR to accommodate ASTER, ETM+ and MODIS sensors.

7) Accessibility of the site and distance from Tucson are also important factors. Many of our field measurements are supported by a mobile laboratory which requires passable roads.

There is no ideal calibration site that satisfies all of the above conditions. Furthermore, no one site can satisfy the requirements of all MODIS bands simultaneously. Obviously trade-offs among different sites will be made. In the Southwestern United States there exist several fairly uniform reflectance sites which have been used over the course of many years by the RSG for calibrations of Landsat-TM, SPOT-HRV, and other airborne and satellite-borne imaging sensors.

3.2 White Sands Missile Range

The White Sands Missile Range test site has been in use for vicarious calibration since the mid-1980s. It is located in the desert southwest of the United States in a region of low aerosol loading and an elevation of 1.2 km. The test site used for small footprint sensors is commonly referred to as Chuck Site and is located in the alkali flats region. This area is relatively devoid of vegetation. The surface near the test site includes regions of greater vegetation and large gypsum dunes. In the VNIR, the White Sands site has a fairly flat spectral reflectance that is quite high, however, the reflectance is much lower and spectrally structured in the SWIR (see

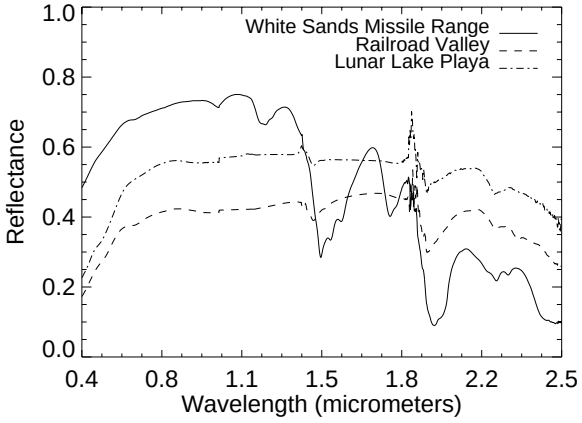

Figure 3-1. Results of spectral reflectance measurements of vicarious calibration sites

figure 3-1). The level of reflectance varies with season with the lowest reflectance values during the winter months when portions of the test range are either underwater or wet from the higher water table. Highest reflectance values are typically seen in late fall after the surface has dried after summer-season rains.

3.3 Playa-based sites

Ivanpah Playa, Lunar Lake Playa, and Railroad Valley Playa are dry lakebeds whose composition is dominated by clay. This provides reasonable reflectance levels and small spectral variations in the VNIR and SWIR. These are desert sites where the aerosol loading of the atmosphere is typically low with correspondingly reduced corrections. Railroad Valley in Nevada is the largest of the playa test sites, but is still only one-fourth of the area of White Sands. While the spectral reflectance of the playa sites is much lower than that of White Sands in the blue part of the spectrum, the spectral reflectance is reasonably flat over most of the VNIR and SWIR (figure 3-1). The Ivanpah Playa test site is at an elevation of 0.8 km and the other two are above 1.3 km so that atmospheric corrections are typically small. All three sites are devoid of vegetation and Lunar Lake Playa, while being the smallest of the sites, is the most spatially uniform of all of the test sites used by the RSG. All three sites suffer from surface moisture affecting the spectral reflectance during winter and early spring. The Lunar Lake site suffers from standing water on the site during late winter and early spring due to runoff of water from local mountains.

3.4 Other sites

For the TIR, Lake Tahoe, at a high altitude in Northern Nevada/California, will be used as the VC site. A large body of water is selected for the TIR VC site because of its uniformity and stability due to its large thermal mass and low thermal conductivity of water. Again the high altitude provides smaller and more accurate atmospheric corrections.

4.0 Prelaunch activities

Pre-launch activities are divided into improvements in field equipment, data collection, and processing methodologies. This work relies on previously-collected data sets to develop, improve, and test the software needed for the vicarious calibration after launch. New field campaigns are used in the pre-launch time frame to test data collection methods, evaluate test sites. Finally, a critical aspect to the prelaunch work has been the development of cooperative efforts with other sensor teams and this has led to a clearer understanding of the uncertainties in the vicarious calibration approaches.

4.1 Field instrumentation

In the past, field-reflectance measurements originally depended on an 8-channel radiometer that nominally duplicated the TM bands. More recently, we have begun to use Analytical Spectral Devices FieldSpec FRs that give 1.4-nm spectral resolution from 350 to 1000 nm and 10-nm resolution for the 1000-nm to 2500-nm spectral range. These hyperspectral surface reflectance data have been used in a modified version of our radiative transfer codes to allow us to do hyperspectral, reflectance-based calibrations (Thome et al., 1996). The advantage to this approach is that multiple bands of multiple sensors, such as all VNIR and SWIR bands of ASTER, MISR, MODIS, and ETM+ may be simulated with these data sets.

Diffuse-to-global measurements used in the irradiance-based approach were originally made with a radiometer viewing a reflectance panel. To make the diffuse measurements, we shaded the reflectance panel with a large parasol to block the direct solar irradiance. Global irradiance measurements were recorded without shading the panel. This method is labor-intensive and has large variability due to the difficulties in repeatably blocking the sun. A new instrument, recently developed (Crowther, 1997), improves the repeatability of the diffuse-to-global measurements. This system is similar to shadow-band radiometers (Harrison et al., 1994) but uses a disk to block the sun to reduce the amount of diffuse radiance blocked while occulting the sun. The device collects the downwelling irradiance with an integrating sphere, and a LiCor, LI1800 spectrometer is the detector system. Global and diffuse irradiance can be measured at 1-nm intervals from 300 to 1100.

Other work done during the prelaunch phase of the Terra program included testing a solar radiometer for use in the SWIR spectral range (Sicard et al., 1997), developing a solar-aureole camera (Grotbeck and Santer, 1993), and preliminary testing of a 2-D, CCD array coupled with a fish-eye camera lens for measuring the surface bidirectional reflectance factor (BRF). In addition we obtained a mobile laboratory that includes two, 10-kW generators for use at remote field locations.

4.2 Field data

Field campaigns have been held periodically during the prelaunch phase of Terra. These campaigns have typically been associated with overpasses of Landsat-5 TM, SPOT HRVs, and the AVIRIS and MAS airborne sensors. More recent campaigns have included data sets collected during overpasses of AVHRR, Vegetation, and SeaWiFS that are used to simulate the larger footprint size of MODIS.

4.2.1 Reflectance-based method

The prelaunch field campaigns using reflectance-based data have focused on improving and refining our measurement techniques for small-footprint sensors. In addition, we have investigated the feasibility and methodology to extend this method to the large footprint size of MODIS. Our current approach for small footprint sensors is to measure an area of the order of 120 m × 480 m. This area is broken into 64 sub-areas that are 30 m × 30 m and 10 samples are collected within each of these sub-areas while walking a straight line through the center. This process takes approximately 50 minutes and this length of time is typically short enough to reduce effects from changing solar angles and atmospheric conditions. The total distance walked in this situation is 1.2 km and the length of time is defined by the data collection rate of the spectroradiometer. For a large footprint sensor such as MODIS, we could continue to sample the site in an identical fashion and assume that these measurements of the small 120-m × 480-m area are applicable to a much larger area related to a 1-km pixel. This method is adequate for several areas of the Railroad Valley Playa and White Sands Missile Range. However, this would require moving the small-footprint test sties for which there is an historical set of measurements, and this is not desirable at this point for reflectance-based calibration of the small-footprint sensors.

Another approach is to sample a larger area of the test site with the same philosophy that is currently used. Obviously, dividing the site into 30-m subareas is not feasible since it would require measuring more than 1100 subareas to cover a 1-km pixel and take more than 14 hours. A more reasonable approach is to subdivide the large area into the same 64 pixel subareas collecting 10

samples within each area. The smallest preferred size of the overall site would be 1.5 km × 1.5 km so as to allow us to characterize some of the uncertainty from misregistration of the ground-based measurements to the MODIS pixel being calibrated. In this case, each subarea is about 190 m × 190 m and the samples would be approximately 19 m apart in the "along-track" direction and 190 m in the "cross-track" direction. This approach still has two problems. First it is logistically difficult to transport the reference standard that is used to convert these data into reflectance over the distances that are necessary in this case. Second, and more importantly, is that the total distance walked is 8×1.5 km or 12 km. This would take someone walking at a rapid pace about 2 hours to complete and this is longer than desired.

If we wish to keep the measurement time to about one hour, then we are limited to about 6 km of linear distance. In order to sample a 1.5-km × 1.5-km, we are now limited to four transects through the area. One option is to have all four lines parallel to one another. This has the logistical problem of moving the reference standard. The approach that has been adopted is to have two pairs of transects where the pairs are oriented 90° to each other and oriented approximately in the along- and cross-track directions. For logistical reasons, we separate each transect within a pair by only about 150 m to simplify the reference measurements. This approach has the advantage of attempting to characterize broad scale changes in the site in orthogonal directions. The disadvantage to this method is that the sampling could be inadequate to properly characterize the reflectance of a full MODIS pixel.

Such an approach was tried during a calibration campaign to White Sands in April 1998 for the sensor Vegetation. Figure 4-1 shows the average spectral reflectance for the two north-south lines that were walked as well as the average reflectance for the two east-west lines. The dotted line in the figure shows the relative difference between the two curves. As can be seen from this figure, the spectral reflectance between the two orthogonal paths is significantly different in the shortwave IR. To further show this effect, Figure 4-2 shows the spatial reflectance for each of the four lines for a wavelength of 2300 nm. While the two north-south lines are relatively flat spatially, the east-west lines show distinct changes in the surface reflectance. Examination of high-spatial resolution satellite imagery after the campaign also showed this effect. The conclusions from such data are that the reflectance derived in bands 0, 2, and 3 of Vegetation would have slight errors due to spatially varying surface reflectance while the band in the shortwave IR, band 4, would have significant uncertainties.

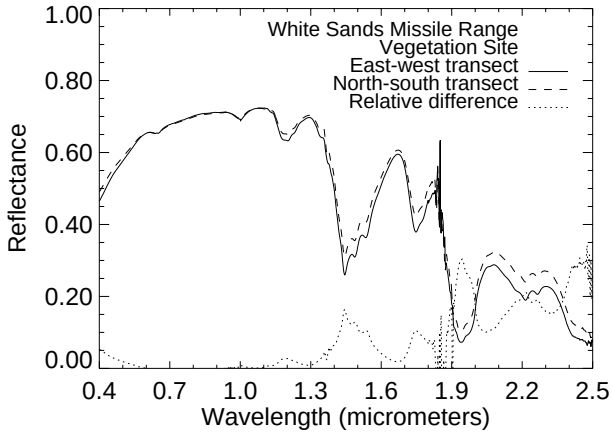

Figure 4-1. Spectral reflectance for average of north-south and east-west transects. Also shown is the relative difference between the orthogonal data.

One way to avoid the sampling strategy problem is to fly an aircraft at low-altitude over the site to collect reflectance data.

This approach has the advantage of being able to sample a much larger area in a short period of time. Successful data collections of this type have been collected at Railroad Valley and are currently under evaluation. The sampling strategy adopted in this case was to fly 18-km long lines in the along-track direction of the satellite. A 4-km wide area of the ground was sampled using seven flight lines. The center five lines were separated by 500 m with the two outer lines being 1 km from the outer lines of this central region. Such a sampling took approximately 45 minutes.

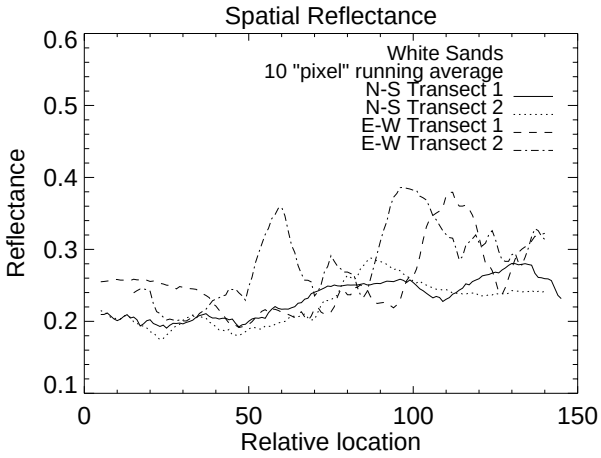

Figure 4-2. Reflectance as a function of location for each of the four lines of the Vegetation site at White Sands at a wavelength of 2300 nm.

4.2.2 Irradiance-based method

Preflight work on the irradiance-based approach has focused on tests of the newl-developed diffuse-to-global meter. The system was shown to retrieve spectral optical depths to within 0.01 of those from a well-understood solar radiometer (Smith et al., 1998). The system has also been used as part of calibrations involving Landsat-5 TM and AVIRIS using our White Sands and Lunar Lake test sites. An example of results from the newly-developed diffuse-to-global meter are shown in Table 4-1 that shows radiances derived from both the reflectance- and irradiance-based results compared

Table 4-1.
Comparison predicted radiances for TM from reflectance- and irradiance-based approaches and those determined from image data DNs and NLAPS gains and biases

TM Band	Radiances ($W/m^2/sr/\mu m$)			Average site digital numbers	NLAPS gain ($W/m^2/sr/\mu m$/ DN)	NLAPS bias ($W/m^2/sr/\mu m$)
	Reflectance-based	Irradiance-based	Image-based			
1	136.6	128	121	203.3	0.602	-1.52
2	137.1	130.9	115.2	100.5	1.175	-2.84
3	127.5	124.4	112.5	141	0.806	-1.17
4	94.95	94.12	87.96	109.8	0.814	-1.51
5	17.76	-	12.23	116.6	0.108	-0.37
7	1.782	-	1.795	34.1	0.057	-0.15

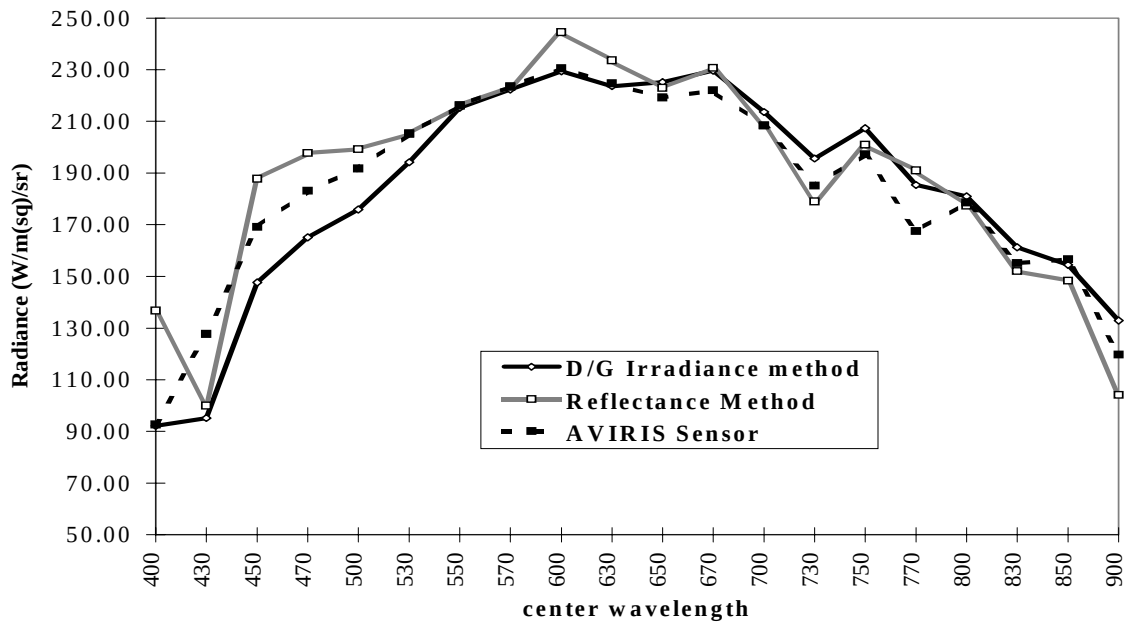

Figure 4-3. Reflectance- and irradiance-based results from Lunar Lake Playa compared to measured radiances by AVIRIS.

to those reported by the Landsat-5 TM sensor. The differences between the two are on the order of 1-6% and these are within the method's combined uncertainties. From the table it is clear that there is better agreement between the irradiance-based method and the image data. However, with the exception of band 5, the differences between all three methods are <15%. When the 10% uncertainty of the image data is considered, the results shown are within the combined uncertainties of all three sets of results. Results from the comparison with AVIRIS are shown in Figure 4-3 and show similar results as those from the Landsat case.

4.2.3 Radiance-based method

Tests data were also collected for the radiance-based method. An example of results from the radiance-based approach is given in Table 4-2 for data collected during a campaign to Lunar Lake, Nevada. In this table are the predicted radiances at aircraft level based on the results of a reflectance-based calibration and those measured by the radiometer at aircraft level. This was done for two altitudes, 6,200 and 10,700 feet above mean sea level (or 700 and 5,200 feet above ground level). As can be seen, there is excellent agreement in all bands but the first. A possible explanation for this difference is that the lamp used to calibrate the airborne radiometer does not have high output in the blue end of the spectrum, making the calibration less accurate.

When applying the radiance-based method to MODIS, a similar sampling problem as that of the reflectance-based is encountered. Typically, the radiance-based approach is applied by flying a radiometer in a light airplane or helicopter. Thus, it becomes straightforward to characterize a larger area, since the aircraft can cover a large area in a short time. Again, the tradeoff is between the

Table 4-2.
Comparison of radiances predicted at aircraft level for two altitudes based on reflectance-based and radiance-based measurements

Exotech Band	Wave-length (nm)	Radiances at 6,200 ft MSL $W/m^2/sr/\mu m$			Radiances at 10,700 ft MSL $W/m^2/sr/\mu m$		
		Radiance-based	Reflectance-based	% diff.	Radiance-based	Reflectance-based	% diff.
1	486	147	169	15	145.3	162.9	12.1
2	549	199.9	201	0.6	195.1	191.7	-1.7
3	653	210.5	212.6	1	204.6	202.4	-1.1
4	840	149.6	154.1	3	145.2	146.1	0.6

amount of time to sample the site versus the frequency of the sampling. For this discussion, we assume that temporal effects due to changing sun angle can be corrected. Changes in atmospheric conditions between overpass and the aircraft measurements are more difficult to correct, especially if the aircraft is covering a large geographical area.

The sampling strategy adopted during a June 1998 campaign to Railroad Valley was to fly seven lines parallel to the along-track direction of the satellite. Each line was 18 km long and flown at an altitude of 3900 m above sea level. The lines were separated by 1 km and the entire data collection required 45 minutes. The center line of the flight was timed so as to coincide with the overpass of the satellite sensor. The center five lines of this flight coincided with low altitude lines of the reflectance measurements described above allowing for comparisons of the two data sets. These data will be compared to the HRVIR imagery to determine if this sampling strategy is sufficient to characterize the playa. If not, shorter lines, spaced closer together could be used. However, the longer flight lines offer an opportunity to use the least spatially varying portions of the playa without a priori knowledge of the spatial homogeneity.

4.2.4 Cross-calibration method

Cross-calibration studies during the prelaunch phase concentrated on demonstrating the feasibility of such a method using small-footprint sensors. The philosophy being that if it is not possible to achieve suitable accuracy with these sensors, then it would not be possible for large footprint sensors. As an example of a portion of the work done in this area, we studied data from Landsat-5 TM and SPOT-3 HRV of White Sands on October 8 and 9, 1994 respectively. The atmospheric conditions on both days were measured as was the surface reflectance of the test site. These data were used to determine reflectance-based calibrations of both sensors. The cross-calibration used

bands 2, 3, and 4 of TM matched with bands 1, 2, and 3 of HRV respectively. Though not identical, these pairs of bands are quite similar. The difference in reflectance between bands was determined from FieldSpec FR data. To account for pixel size differences, each pixel for both sensors was divided to create 10-m × 10-m pixels.

The HRV image was twisted and resampled using nearest-neighbor resampling to register it to the TM image using nine ground-control points. The HRV data were converted to radiance using reflectance-based calibration coefficients derived from data collected during the sensor overpass. The SPOT data for the alkali flats area were atmospherically corrected using the ground-based atmospheric data from this reflectance-based calibration to retrieve the surface reflectance for the three HRV bands.

Two types of test sites were selected from the SPOT data set for cross-calibration purposes: 1) the test site used for reflectance-based calibrations; and 2) 90-m x 90-m areas in the TM image (9-pixel areas) for which there were no variations in DN. Once a site was selected, the average reflectance from HRV data was found for 80-m x 80-m areas encompassed by the TM area. The reflectance for each of the TM bands was determined using the reflectance of the corresponding HRV band. Results were determined by either assuming that any spectral differences were small enough to ignore, or accounting for spectral differences using measured spectral reflectance data collected at the reflectance-based site. The TM reflectances were converted to radiance by reversing the atmospheric correction using ground-based atmospheric data from the day of the Landsat-5 overpass. These radiances were compared to the average DN of the 9-pixel area to determine the calibration coefficient.

We applied this approach to numerous areas in the White Sands area. For brevity, we give the results for four representative areas: the reflectance-based calibration site, a dune area and two darker alkali flat areas. Table 4-3 presents the percent difference between the TM calibration coefficient obtained from the cross-calibration to HRV and those obtained from the reflectance-based approach. Two sets of results are given for Chuck Site. The first is with no spectral correction and the second includes a spectral correction based on ground-based reflectance measurements collected at the reflectance-based site. The dune target is about 20 DN brighter than the reflectance-based site and both of these sites give similar results indicating the

Table 4-3. Table showing percent difference between calibration coefficients derived for TM using the reflectance-based approach and the cross-calibration approach using HRV data.

Site	HRV 1 TM 2	HRV 2 TM 3	HRV 3 TM 4
Chuck Site w/o spectral correction	4.3	0.9	0.1
Chuck Site w/ spectral correction	0.3	0.4	0.2
Dune Area	4.2	1.2	1.1
Dark Area 1	3.4	3.2	1.6
Dark Area 2	13.9	12.7	7

similarity in spectral reflectance between the two areas. The last two areas are very similar to each other, both with average DN values about 13 DN less than the reflectance-based site. The fact that the first dark area gives reasonably good results while the second dark area does not, could be due to vegetation in the second dark area. These last two targets used in the comparisons show the importance of properly assessing the effects of spectral differences between sensors.

Even though the overpasses occurred on different days, this was not a problem because of the near-lambertian quality of the site and the similar view/solar geometry of the sensors. Results of the cross-calibration show we can retrieve TM calibration coefficients, using HRV, to < 1% of the reflectance-based values when band-to-band differences in the spectral reflectance are taken into account (Gustafson-Bold and Thome, 1996).

4.2.5 Laboratory improvements

It should be pointed out that the cross-calibration results presented in the previous section do not include the uncertainty in the radiance calibration of the reference sensor (HRV in this case). This is because the same calibration approach was used to determine the calibration of HRV as was used to determine the calibration of TM to determine the differences shown in Table 4-3. Thus, any bias in the approach is in both the calibration of TM and HRV. A true test of this approach requires comparisons to use independent calibration methods. Still, the results in Table 4-3 are encouraging and definitely show the utility of cross-calibration.

One way to use independent calibration methods, yet still ensure consistency in the conversion to absolute radiometric units is through two stable, precise, and accurate transfer radiometers built by the RSG during the prelaunch phase. One of these radiometers has seven bands in the VNIR and the other has nine bands in the SWIR. These CCRs (cross-calibration radiometers) were designed to measure the radiance of the various sources used to radiometrically calibrate EOS sensors. The VNIR radiometer is based on a temperature-stabilized, silicon, "trap" detector (Zalewski and Duda, 1983) with the only optics being interference filters and field-of-view determining apertures (Biggar and Slater, 1993). The SWIR radiometer is based on a liquid-nitrogen-cooled, indium-antimonide detector with a filter, field-of-view determining apertures, and a cold filter (Spyak and Lansard, 1997). Both radiometers were systematically characterized for field-of-view, spectral response, stability, and repeatability and were calibrated radiometrically by reference to a NIST-calibrated standard of spectral irradiance.

The VNIR CCR has been used to determine the output of the 100-cm SIS for the calibration of MODIS and SeaWiFS, the 100-cm SIS for the calibration of the VNIR portion of ASTER, the 165-cm SIS for the calibration of the MISR cameras, and the 48" SIS for the calibration of the Landsat 7 ETM+. This CCR has also been used to measure the output of the 200-cm SIS used in the calibration of OCTS and the SIS for the SPOT HRV cameras. The SWIR CCR measured the 100-cm, MODIS SIS, the 100-cm SIS for the SWIR portion of the ASTER instrument, and the 48" SIS of Landsat 7 ETM+. The results of these measurements have been provided to the EOS Calibration Scientist and should be helpful in determining biases between the calibrations of these sensors.

Additional work with the VNIR CCR has been to perform solar-radiation based calibrations using techniques similar to those used to calibrate the SeaWiFS (Biggar and Slater, 1993). In a solar-radiation-based calibration, the sensor views a panel of known reflectance that is illuminated by the sun. The amount of signal from diffuse illumination from the sky is determined by shading the panel from the direct-solar beam. Subtracting the diffuse-skylight irradiance reflected by the panel from the global irradiance reflected by the panel gives the radiance from the panel due only to solar illumination. The predicted radiance from the panel is found from knowledge of the panel's BRF and the incident solar irradiance. The panel BRF is determined in our calibration laboratory.

The solar irradiance is found using measured atmospheric transmittance using solar radiometers. An inversion technique is used to determine the spectral transmittance at wavelengths not measured by the solar radiometer channels. The incident irradiance is determined by multiplying appropriate values of the solar spectral irradiance by the spectral transmittance. This approach will allow us to determine the bias between the sources used in the preflight calibration of the ESE sensors and that of the data collected in flight. Table 4-4 provides an example of results showing differences between radiances measured from a reflectance panel, calibrated in our laboratory, using the VNIR CCR and those predicted from two sets of solar irradiances. The agreement for some of the bands is quite good, but it is clear that there are some larger differences that need to be examined to ensure consistency between laboratory calibrations and data collected under solar illumination.

4.3 Joint campaigns

As a means to understanding the accuracy of vicarious methods, the RSG has organized several joint campaigns to the Nevada test sites and participated in a joint campaign to Japan. The purpose of these campaigns was to collect coincident data sets with several groups and compare the results of these measurements at various stages of the processing sequence to determine the causes of significant differences in predictions of TOA radiances. As an example of this work, results from a field campaign to Lunar Lake, Nevada in late May, early June 1996 are shown here. This campaign included VC teams from ASTER, MISR, MODIS, and ETM+. The members from ASTER included both Japanese and US team members.

Table 4-4
Percent differences between measured radiances from a reflectance panel and those predicted from solar irradiance tables of Neckel and Labs (1981) and Thuillier et al. (1997)

Source of Solar Irradiance	Percent difference for the given wavelength (nm)						
	412	442	488	531	678	748	869
Neckel and Labs	-0.8	-2.11	-3.55	-0.75	0	-1.57	-0.56
Thuillier et al.	2.05	-0.35	-0.42	0.32	-0.1	-0.28	N / A

For comparisons of predicted radiances, we concentrated on a data set from 1800 UTC on June 2, 1996. The normalized-radiance results from this time are shown in Table 4-5. We use normalized radiances here to avoid differences in assumed values for the exoatmospheric solar irradiance that led to as much as 3% differences in predicted TOA radiance. The results are for a set of "monochromatic" wavelengths at 450, 550, 650, 800, 1000, 1600, and 2200 nm, as well as a set of six rectangular bands with center wavelengths at 399, 562, 812, 1027, 1688, and 2217 nm and bandwidths of 10, 100, 100, 10, 100, and 100 nm respectively. These wavelengths and bands sample the solar reflective portion of the spectrum while avoiding regions of strong atmospheric absorption. The JAC are from the Japanese ASTER Calibration team and are reported only for the VNIR because their spectrometer covering the shortwave infrared did not operate after shipping to the United States. The results indicate that the RSG results are slightly higher than those of the other groups and this difference is larger at longer wavelengths. There is also a trend to the results of the JAC group with differences becoming larger with wavelength. These results are typical of those from other days and times.

Table 4-5. Predicted normalized radiances at the top of the atmosphere over the Lunar Lake Playa target at 1800 UTC on June 2, 1996.

Central Wavelength (µm)	Normalized radiance			
	MISR	JAC	SDSU	RSG
Rectangular Bands				
0.399	0.078	0.0766	0.073	0.0792
0.562	0.1069	0.104	0.1005	0.1112
0.812	0.1384	0.126	0.1309	0.1367
1.027	0.1391		0.1379	0.1495
1.688	0.1371		0.1344	0.1393
2.217	0.1157		0.1127	0.1167
Monochromatic Values				
0.45	0.086	0.0848	0.0805	0.0876
0.55	0.1041	0.1025	0.0992	0.109
0.65	0.1249	0.1193	0.1211	0.1287
0.8	0.1383	0.1332	0.1366	0.144
1	0.1362		0.1378	0.1431
1.6	0.1379		0.1315	0.1342
2.2	0.1161		0.1121	0.1108

Examination of the results from this work revealed that a significant source of difference seen in the normalized-radiances are differences in retrieved surface reflectance. Table 4-6 gives the retrieved reflectances used to derive the results in Table 4-5. Two sets of results from the RSG are shown in this table with one set based on FieldSpec FR data and the other from an eight-band radiometer. The correlation between the percent differences is expected because the high surface reflectance and low turbidity means that the at-sensor radiance is dominated by the reflected radiance from the surface. Past work by the RSG estimates that the uncertainty of its surface reflectance retrieval for a site such

as Lunar Lake is 2%, or 0.01 in reflectance, at a reflectance of 0.5. This same work also shows that for high-reflectance targets, the uncertainty in the at-sensor radiance due to uncertainty in the reflectance are roughly the same. That is, a 2% uncertainty in reflectance leads to approximately a 2% uncertainty in at-sensor radiance. While the agreement in reflectance between the groups is quite good, the between-group differences are larger than what would be expected with this level of uncertainty.

Table 4-6. Measured reflectances of the playa site used to determine predicted, normalized radiances at the top of the atmosphere at 1800 UTC on June 2, 1996.

Central Wavelength (µm)	Reflectance				
	MISR	JAC	SDSU	RSG FR	RSG MMR
Rectangular Bands					
0.399	0.205	0.205	0.207	0.218	0.200
0.562	0.393	0.398	0.389	0.410	0.412
0.812	0.488	0.481	0.491	0.519	0.517
1.027	0.489		0.497	0.530	0.525
1.688	0.482		0.492	0.512	0.513
2.217	0.407		0.425	0.441	0.459
Monochromatic Values					
0.45	0.266	0.274	0.268	0.282	0.270
0.55	0.375	0.386	0.378	0.397	0.402
0.65	0.453	0.454	0.452	0.478	0.479
0.8	0.488	0.485	0.491	0.521	0.516
1	0.479		0.494	0.510	0.525
1.6	0.486		0.492	0.517	0.516
2.2	0.411		0.418	0.429	0.485

Sampling of the playa is not a primary cause of the differences since there is good agreement between the two RSG instruments that were operated independently. Additionally the standard deviation of the average of 700 spectra from the RSG's ASD FR collected over the entire 64-pixel site is less than 1.5% for all spectral ranges not affected by absorption. This is a good indication of the level of uniformity of the target. The types of reference panels was also not a major source of difference, but the manner that these reference panels are calibrated and how they are used is the source of the differences. The method used by the RSG is unique from the other three in that the RSG measures the bi-directional reflectance factor (BRF) of the field reference prior to, and after, each field campaign. The reflectance of each playa sample is determined by computing the BRF of the reference panel for the solar geometry of the measurement based on the time of the measurement. This has the advantage of both accounting for changes in the panel reflectance as a function of solar incidence angle, as well as correcting for effects due to the cosine of the angle of the incident solar beam. The other groups used the spectral reflectance of their reference as determined from the

hemispheric-directional reflectance factor (HRF) rather than the BRF. Their approaches do not include changes in the HRF due to the changing solar zenith angle, nor is there a correction for the cosine of the solar zenith angle. For the MISR group, this cosine correction is not important since the reference panel and playa measurements were collected within a minute of each other. For the JAC and SDSU groups, the time between panel and site measurements could cause as much as a 1% change.

To examine the effect of using HRF rather than BRF, two tests were done. The first involved determining the reflectance of the UA's barium sulfate reference at the monochromatic wavelengths using measurements by the SDSU group. The results of this comparison showed differences of 6% to 8% with smaller differences at longer wavelengths. The second test consisted of processing data collected by the RSG with a monolithic Spectralon® panel using both the HRF and the BRF. The percent difference between these results was also in the 5% range. indicating that much of the difference between the two groups can be attributed to the use of the BRF by the UA group and the HRF by the MISR group.

The difficult question that must be addressed is whether to use HRF or BRF? In reality, neither is strictly correct because there is a significant diffuse component from the sky that prevents the situation from being truly bi-directional. This is especially true in the "blue" bands of ASTER, ETM+, MISR, and MODIS where the diffuse skylight accounts for as much as 10% of the reflected signal for the data shown here. The strong directional component from the sun and the sky radiance as a function of zenith and azimuth angle makes it complicated to treat the problem as hemispherical-directional. One can make used a parasol to collect measurements while shading the panel and playa to create a set of bi-directional data, but this is unwieldy on a large scale and does not truly simulated the "reflectance" seen by the satellite which includes the hemispherical component due to skylight.

An additional source of the differences in TOA radiance are the atmospheric characterizations. One specific cause is the difference in aerosol optical depth for each of the bands. For all but one of the groups, the differences in derived optical thickness were less than 0.01. The results showed that the differences in the at-sensor radiance due to optical depth differences are less than 0.6%. Similarly, there were differences in retrieved aerosol size distribution and these led to differences of less than 0.7%. When the optical depth and aerosol size distribution differences are coupled, as they are physically, the difference in TOA radiance is less than 0.5%.

The final aspect of the processing that was examined was the effect of the radiative transfer codes. Ideally, a methodical comparison of all of the codes used for this work should be done. However, it is still possible to obtain an idea of the effect expected from using different radiative transfer codes by comparing the results obtained by one radiative transfer code relative to results reported by each group. For this, the monochromatic bands at 450 and 1000 nm were selected because gaseous absorption effects are negligible for these two bands. These two bands also give cases of high and low scattering optical depths.

The RSG code was run using the inputs from the JAC, MISR, and SDSU groups. The differences between the Japan and UA codes do not appear significant for the one band examined and indicate that the 1% stated uncertainty for the Gauss-Seidel is reasonable. This 1% uncertainty appears too small for the SDSU and JPL cases at the shorter wavelength where differences of 3-4% were seen. Differences in the codes are expected to be larger for the shorter wavelength because of the larger dominance of scattering at this wavelength. However, the good agreement at the longer wavelength, indicates that when care is taken to ensure that the aerosol index of refraction and aerosol phase functions are handled consistently between groups, the radiative transfer codes are not a significant source of difference in vicarious calibration. This is especially true when one considers that vicarious calibration is typically done over bright targets with low aerosol loading.

4.4 Uncertainties

The results of the prelaunch field campaigns have led to a clearer understanding of the uncertainties of the vicarious methods. These are discussed here for all four of the methods that will be used for MODIS.

4.4.1 Reflectance-based approach

Table 4-7 lists the error sources we have identified for a wavelength region in the green portion of the visible spectrum corresponding to band 4 of MODIS. The error column is the percent error in the quantity listed in the source column. The total error column is the error in TOA radiance in percent at the sensor caused by the item in the source column. The total is the root sum of squares of all the error sources. The choice of the root sum of squares is not necessarily valid as the sources are not known to be independent.

These uncertainties clearly depend on wavelength with larger uncertainties in spectral regions with strong absorption. For example, the uncertainty in the atmospheric correction increases with shorter wavelengths and the ozone correction is very small or insignificant at longer wavelengths. The results in the table are for a typical calibration day for our current test sites: cloud free with visibility of 50 km or more.

As seen from the table, the largest sources of error are in the atmospheric characterization and the surface reflectance retrieval. In our modeling of the atmosphere at White Sands, we have typically chosen an index of refraction for the aerosols of 1.44-0.005i. RTC results, with the index varied as a parameter and other inputs appropriate for a typical White Sands day show differences in TOA radiance of 1.7% to -1.4% for a change in imaginary part of the index of 0.005 with a ground reflectance of 0.5. The change in the radiance due to a change in the real part of the index is much smaller. The choice of the aerosol particle size distribution also entails a large uncertainty. In past calibration work we used a Jungian distribution to describe the size distribution. In RTC simulations with nominal White Sands conditions, a typical uncertainty of 0.5 in the Junge parameter gives an increase in TOA radiance of 0.5%. More recently, the use of sky radiance measurements and diffuse-to-global irradiance allow for a better determination of the aerosol type that does not rely on the used of a Junge distribution. This approach is still being evaluated, but should improve our knowledge of the complex index and size distribution such that TOA radiance uncertainties will be reduced from their current values of 2.0 and 3.0% respectively to 1.5% and 1.5%

TABLE 4-7

Reflectance-based method error sources, with reference to solar exoatmospheric irradiance. The values are quoted as one-sigma percentages.

Source	Error	Total Error
Aerosol complex index (1.44-0.005i)		1.5
Choice of aerosol size distribution		1.5
Optical depth measurement	5.0	1.0
Column ozone uncertainty	20.0	1.3
Vertical distribution of aerosols		1.0
Inherent RTC accuracy	1.0	1.0
Non-lambertian ground characteristic	1.2	1.2
Ground reflectance measurement	1.5	1.5
Total Error (root sum of squares)		3.6

The RTC used in our calibrations requires optical depth components due to molecular scattering and aerosol scattering and absorption. The starting point for determining these optical depths is the measured extinction optical depth. The accuracy of this measurement depends on the calibration of the solar radiometer and the stability of the atmospheric conditions during the period of measurements. For a carefully calibrated instrument, this error should be no more than 5 percent in optical thickness and less than 1% in TOA radiance. From the spectral optical thickness, we can determine the column ozone amount to within 20%, (Biggar et al., 1990) and this translates to an error of 1.3% in TOA radiance.

There are several other uncertainties related to the RTC. Comparisons between independent codes making similar assumptions (Mie scattering by the aerosols, Junge size distributions, etc) but different numerical techniques, give results which compare at the 1% level. In our work, we use a scalar code that does not account for polarization of the scattered radiation but have found the TOA radiance changes by less than 0.1%. This is an insignificant error as long as the sensor being calibrated is not sensitive to the polarization of the light incident at the sensor. If this is not the case,

the polarization code will be used and the polarization characteristics of the sensor must be well understood to eliminate calibration errors.

Another consideration is the accuracy of the measured surface nadir reflectance factor. We estimate the directional reflectance error of the field standard is no more than 1.5% and the precision of the radiometer measurements of the sand and the standard are 0.5% due to sampling errors and limitations of the instruments and data loggers. We correct the nadir reflectance factor for the component of diffuse light in the field which is not present during the laboratory calibration of the standards. This correction has an uncertainty of about 0.5%. In addition, their is the uncertainty due to

We must recognize that the total of these errors could add to much more than the root sum of squares. Also, these are in reference to the exoatmospheric solar irradiance and as shown in Table 4-5, there is still significant uncertainty in the conversion from relative radiance to absolute. There are also several other sources for additional uncertainty when applying a reflectance-based approach to MODIS. One source is that the atmospheric data must be assumed to be constant over a much larger area. This should not cause too much of a problem since typical calibration days have non-varying atmospheric conditions. However, this effect can be significant in the case of cloudy conditions, especially those for which there would be sub-pixel clouds. Additional uncertainties arise from MODIS's large field of view allowing it to image White Sands as often as three consecutive days and up to four consecutive days at Railroad Valley. This large field of view implies large view angles, and these large view angles require a much better characterization of atmospheric effects due to the longer view path and an improvement in the characterization of the surface bi-directional reflectance. Both of these problems have been decreased somewhat through the development of new field instruments to characterize atmospheric effects and surface bi-directional reflectance. In addition, there will be a larger uncertainty in the reflectance retrieved for application to MODIS. This will not cause significant problems in future work as a better understanding of the spatial nature of the reflectance is gained through repeated work at the test sites.

4.4.2 Irradiance-based approach

The improved reflectance-based method uses many of the measurements made for the basic reflectance-based method along with the measurement of the diffuse-to-global irradiance ratio at the ground. The errors and the estimated values are given in Table 4-8.

In the improved method, two quantities are calculated by the radiative transfer code that were not explicitly used in the reflectance-based method. The computation of the spherical albedo and the atmospheric reflectance depend on the atmospheric model chosen. The choice of the wrong model for equivalent conditions at White Sands can give an error of up to 1%. These two terms are normally of opposite sign however and an error in one is usually counterbalanced to a degree by an opposite error in the other. As the terms enter directly into the computation of the apparent reflectance (which is directly proportional to the TOA radiance), the error in either term contributes to an error of the same sign and amount in the calibration.

TABLE 4-8.

Irradiance-based method error sources, with reference to solar exoatmospheric irradiance. The values are quoted as one-sigma percentages.

Source	Error	Total Error
View and solar transmittance	1.5	1.5
Surface reflectance measurement	1.5	1.5
Spherical albedo and atmospheric reflectance		1.0
Diffuse-to-global ratio measurement	2.7	1.7
Total Error (root sum of squares)		2.9

The largest error source in the improved method relates to the measurement of the ratio of diffuse to global (total) irradiance. Careful study of the recently-developed diffuse-to-global meter shows that the measurements of this system are accurate to better than 2.7%. This gives rise to an error of about 1.7% in TOA radiance.

4.4.3Radiance-based approach

The sources of uncertainty for the radiance-based method are listed in Table 4-9. The largest error is the calibration of the radiometer. One source of uncertainty in calibrating the radiometer is the lamp used as the spectral irradiance standard suffers from both scale and transfer uncertainty as

TABLE 4-9.

Radiance-based method error sources. The values are quoted as one-sigma percentages.

Source	Error	Total Error
Radiometer calibration	1.6	1.6
Data logger accuracy	0.5	0.5
Radiometer stability	0.5	0.5
Registration	1.8	1.8
Atmospheric correction for altitude difference	5.0	< 0.1
Total Error (root sum of squares)		2.5

given by the calibration laboratory. In addition, we use a standard reflectance panel in our calibration of the radiometer so that we can calibrate in a radiance mode as opposed to irradiance. This panel directional reflectance is known to no worse than 1%. These uncertainties, coupled with other lesser uncertainties lead to the 1.6% overall uncertainty in the radiometer.

The other uncertainties listed in the table result from the use of the radiometer to predict the TOA radiance above the test site being measured. This includes errors due to scaling the radiance measurements to the scale of a MODIS pixel, pointing differences between the airborne and satellite sensors, and the data collection electronics.

4.4.4Cross-calibration approach

If MODIS is cross-calibrated by reference to another satellite sensor, the uncertainties are similar to those shown in Table 4-9 for the radiance-based method. However, the reference radiometer will most likely have larger uncertainty than the 1.6% given in this table. Data logger accuracy and radiometer stability are no longer a factor, but the atmospheric correction is more important, causing up to a 0.5% uncertainty. BRDF effects will be present for the ETM+ to MODIS case, but the near-lambertian quality of our test sites should make this negligible.

The two most important possible sources of uncertainty in the cross-calibration of MODIS using ASTER/ETM+ will be due to registration of the data sets and the spectral mismatch of the sensors. To examine registration effects, we used both the TM and HRV imagery from the October 1994 White Sands dates. The small-footprint imagery were resampled by averaging to create footprints approximately 1 km in size. The 1-km data were then shifted relative to the small-footprint data and new calibration coefficients were computed. In both the HRV and TM cases, several 4-km by 4-km areas were found for which there was less than 1% changes in the computed calibration coefficient for up to a 0.5 km misregistration. Unfortunately, these areas are not the same in all bands, but are slightly displaced from each other. There are also large extended areas, up to 10 km by 10 km in size, for which a 0.5-km misregistration has less than a 3% effect. A similar approach was used on HRV data from November 1995 of Railroad Valley Playa. Much like White Sands, there are several regions of the playa for which there are areas of 9 km^2 where there is no change in calibration coefficient for up to a 0.5 km shift in the imagery. Unlike White Sands, we were not able to find large extended areas for which the misregistration effect is less than 3%.

In addition to misregistration, there are spectral differences between the two sensors. This would still cause a significant uncertainty in cross-calibration, but selection of a suitable target will reduce band-to-band effects to the point of being insignificant. Possible uncertainty due to this spectral effect has been examined using spectral reflectance data from both White Sands and Railroad Valley and spectral response measurements of both sensors. These results indicate that, at least for these spectral reflectance data, the spectral mismatch will not be a primary source of uncertainty except for the shortwave IR band at White Sands. The key to this source of uncertainty will be monitoring the spatial and temporal variability of the spectral reflectance for any target being used so we are confident we understand how best to correct for spectral reflectance differences.

It should also be mentioned that spectral differences between two sensors will also lead to differences because of the spectral nature of atmospheric scattering and absorption. In this case, the bands are similar enough that spectral scattering effects, which are smooth, have little effect. MODTRAN transmittance results have been used to look at effects due to atmospheric absorption, and these are negligible for most bands.

We estimate the error due to the mis-registration between the images should be only 0.5%. Errors due to spectral band mismatch gives an uncertainty of 1.0%, and the errors in the atmospheric correction should be 0.5%. Assuming the case for which ASTER is radiometrically corrected to 4%, it should be possible to radiometrically calibrate MODIS to better than 4.5%. The above discussion has focused on the vicarious calibration in the VNIR, and SWIR. Because work for the thermal portion does not have as long a history of use by the RSG, we do not have a detailed error analysis at this time. However, results from a recent thermal calibration of Landsat-5 TM indicate the method is most sensitive to measurements of the surface temperature and emissivity and inclusion of atmospheric profiles. Secondary effects include more accurately assessing the upwelling and downwelling atmospheric radiances.

5.0 Post-launch activities

5.1 Field campaigns

We have developed a possible schedule for the vicarious calibrations of MODIS on Terra assuming that the overpasses will occur on the same date as Landsat 7. These plans may still be revised based on changes due to locating alternate sites, loss or gain of equipment, and modifications to the methods we use. It should be noted that while this schedule has been developed for Terra, a similar plan can be developed for PM-1 and other follow-on ESE sensors. Scheduling consists of three types of campaigns: extended campaign scenario, short-turnaround scenario, and calibrations of opportunity. The proposed schedule also assumes a July 28 launch of EOS and that ASTER data will become available on Day 53 (September 18 according to current schedule).

A long duration campaign, typically during the summer to take advantage of the availability of students, has been developed for our Nevada field campaigns to minimize the impact of the longer travel distances from Tucson. This scheduling (shown in Table 5-1) can be modified to any set of targets with appropriate modification to the dates. The philosophy of the campaign scenario is to perform a set of intensive field campaigns aimed at getting the highest frequency of calibrations with the smallest amount of travel. The preferred time frame for the first of such campaigns would be starting on September 22 with an overpass of Ivanpah Playa. This schedule can also shift by 16-32 days depending upon the scheduling of acquisitions for ASTER. However, a shift of 32 days places the data collections into late November when the probability of clear skies decreases. The off-nadir views of the targets listed in the table can also shift by plus or minus one day but the above schedule still gives an idea of a possible summer scenario.

The above schedule gives four bright target, nadir-view calibrations with ground-data within a 33-day period. The extended Lake Tahoe period will be used for dark target calibrations of ocean

sensors, including the ocean bands of MODIS, as well as for atmospheric correction validation. The Ivanpah playa calibrations do not offer a good opportunity to do an accurate calibration of 1-km pixels of MODIS due to small size of target, but the off-nadir pointing capability of MODIS allows multiple calibrations at Railroad Valley. The extended campaigns will also be coordinated with overflights of NASA's ER-2 aircraft with AVIRIS, MAS, or MASTER onboard.

Short-turnaround campaigns will also be used with the goal of obtaining a set of calibration data with as few travel days as possible. This means either using a site within 400 miles of Tucson to use the mobile laboratory or more remote sites with a reduced set of equipment without the mobile laboratory. A typical schedule for one of these campaigns is shown in Table 5-2.

Combining these two approaches leads to a scenario of calibrations of ASTER, MODIS, and ETM+ sensors as shown in Table 5-3. The specific dates shown are based on the extended campaign shown in Table 5-1. The cross-calibrations listed will be done both with and without ground-based data. The cross-calibrations that rely on ground-based data will coincide with the field campaigns described above. The specific planning of the short-turnaround campaigns will depend on the success of previous campaigns and also on the rate of change of the calibration of the Terra sensors.

Table 5-1. Summer-scenario campaign schedule

Day	Location	Sensor View Angle	Aircraft
1 (Sept. 22)	Ivanpah Playa	nadir	
4 (Sept. 25)	Lunar Lake and Railroad Valley	off-nadir	
6 (Sept. 27)		off-nadir	
8 (Sept. 29)		nadir	yes
11 (Oct. 2)	Lake Tahoe	off-nadir	yes
13 (Oct. 4)		nadir	yes
15 (Oct. 6)		off-nadir	yes
20 (Oct. 11)		off-nadir	yes
22 (Oct. 13)	Lunar Lake and Railroad Valley	off-nadir	yes
24 (Oct. 15)		nadir	yes
26 (Oct. 17)		off-nadir	
31 (Oct. 22)	Ivanpah Playa	off-nadir	
33 (Oct. 24)		nadir	

Table 5-2. Short-turnaround campaign schedule

Day	Activity	View
1	Travel to site	
2	Calibration	off-nadir
4	Calibration	nadir
4	Travel if successful calibration	
6	Calibration	off-nadir
6	Travel to Tucson	

5.2 Joint field campaigns

This coordination will be of two kinds. The first is to perform joint campaigns with representatives of ASTER, MISR, MODIS, and ETM+ at a minimum. As before the principal reason for these campaigns will be to allow the TOA radiances from several VC teams to be compared. The second kind of coordination will be to use the results from other VC teams to increase the database of ASTER VC results to validate the cross calibration of these sensors. For instance, data collected as part of an independent MISR campaign could be used for the validation of ASTER TOA radiances.

As yet, there are no formal dates set for the joint VC campaigns, but efforts will be made to coordinate these campaigns with the extended campaigns described above. Thus, the first post-launch, joint campaign will be held in late September, early October at the Lunar Lake/Railroad Valley Playa sites.

Table 5-3. Terra calibration schedule

Days since launch	Activity
1	AM-1 launch
53	End of ASTER sensor checkout
57-89	Extended campaign
95-105	Short-turnaround campaign
105-137	Cross-calibration w/o ground data
137-144	Short-turnaround campaign
144-201	Cross-calibration w/o ground data
201-208	Short-turnaround campaign
208-265	Cross-calibration w/o ground data
265-272	Short-turnaround campaign
272-313	Cross-calibration w/o ground data
313-345	Extended campaign
345-441	Cross-calibration w/o ground data
441-448	Short-turnaround campaign
448-547	Cross-calibration w/o ground data
547-554	Short-turnaround campaign
602-681	Cross-calibration w/o ground data
681-713	Extended campaign

5.3 Other satellite data

The cross-calibration technique described relies heavily upon the availability of correlative satellite data. These data are best collected coincident in time and geometry with the MODIS sensor,

5.4 Geometric registration site

This topic is not applicable to this algorithm. Test sites will be located through registration of MODIS data to a high-spatial resolution sensor such as ETM+ or ASTER. On days for which no such data exist, we rely on the uniformity of the site to reduce the effects of misregistration of the data.

6.0 Implementation of validation results in data production

6.1 Approach and role of EOSDIS

We will rely on EOSDIS to assist in providing the image data required from the multiple sensors that will be used for this work. Since we must only coordinate the data collected by our group, we will not require EOSDIS for the processing of our field data. We will, however, rely on EOSDIS to assist with archiving the field data so that other scientists may gain access to the data.

6.2 Plans for archival of validation data

Archival of the validation data will be done at RSG facilities and the ORNL DAAC. The data will be archived in raw and processed format on Sun-based hard disks and 8-mm tapes using UNIX tar commands. Distribution of the data from the RSG will be through ftp access and a word-wide web site currently being developed for the RSG. This site will be used to allow others to see a list of available data, samples of the data, and summaries of the results. The site will also instruct users how to retrieve copies of the data from the ftp site.

7.0 Summary

This document describes the vicarious calibration approaches that will be used by the RSG to validate the radiances of the MODIS sensor. The approaches use test sites located at White Sands Missile Range, New Mexico and several dry lakebeds in Nevada. Four independent methods have been developed for this work and these are the reflectance-based, irradiance-based, radiance-based, and cross-calibration methods. The first three methods require ground- or aircraft-based data to be collected at the test site at the time of sensor overflight but do not require data from other sensors for the calibration. The cross-calibration technique requires data from an additional imaging sensor but do not require ground-based data at the time of overpass. Uncertainty studies of the four methods indicate that the radiance-based method will provide the most accurate results with uncertainties at the 2.5% level with the irradiance- and reflectance-based results having uncertainties of 2.9% and 3.6% respectively. The cross-calibration results are strongly dependent on the uncertainty of the calibration of the reference sensor, but using a sensor with 4% uncertainty as reference, should provide a calibration to better than 4.5%.

This work will begin shortly after the checkout phase of the Terra platform with an extended field campaign planned for the period of September 22 to October 24, 1999. Plans are being made to have this campaign, and subsequent extended campaigns, be part of joint field exercises with other ESE sensor teams to help ensure the consistency of calibration amongst the different sensors.

8. References

Biggar, S. F., J. Labed, R. P. Santer, P. N. Slater, R. D. Jackson, and M. S. Moran, Laboratory calibration of field reflectance panels, *Proceedings of SPIE*, 924:232-240, 1988.

Biggar, S. F., D. I. Gellman, and P. N. Slater, "Improved evaluation of optical depth components from Langley plot data," *Rem. Sens. Env.* **32**:91-101, 1990.

Biggar S. F., R.P. Santer, and P.N. Slater, "Irradiance-based calibration of imaging sensors," *Proceedings IGARSS '90*, Vol I:507-510, 1990b.

Biggar S. F. and P. N. Slater, "Preflight cross-calibration radiometer for Eos AM-1 platform visible and near-IR sources," *Proc. SPIE 1939-24:243-249*, 1990.

Biggar S. F., P. N. Slater, K. J. Thome, A. W. Holmes, and R. A. Barnes, "Preflight solar-based calibration of SeaWiFS", *Proc. SPIE 1939-23:233-242*, 1993.

Crowther, B. G., *The design, construction, and calibration of a spectral diffuse/global irradiance meter*, Ph. D. dissertation, University of Arizona, 140 pp, 1997.

Gellman, D. I., Biggar, S. F., Slater, P. N. and Bruegge, C. J., "Calibrated intercepts for solar radiometers used in remote sensor calibration," *Proc. SPIE* **1493**:175-180, 1991.

Grotbeck, C. and R. Santer, "Solar aureole instrumentation and inversion techniques for aerosol studies: Part 2, data acquisition and inversion," *Proc. SPIE*, **1968**, 1993.

Gustafson-Bold, C. L. and K. J. Thome, "Cross-calibration of two small footprint sensors," *International Geoscience and Remote Sensing Symposium*, Lincoln, Nebraska, pp. 1283-1285, 1996.

Hovis, W. A., J. S. Knoll, and G. R. Smith, "Aircraft measurements for calibration of an orbiting spacecraft sensor," *Appl. Optics*, **24:**407-410, 1985.

Herman, B. M. and S. R. Browning, "A numerical solution to the equation of radiative transfer," *J. Atmos. Sci.*, **22**:559-566, 1965.

Iqbal, M., *An Introduction to Solar Radiation*, Academic Press, New York, pp. 379-381, 1983.

Neckel, H. and D. Labs, "Improved data of solar spectral irradiance from 0.33 to 1.25 μm," *Solar Physics*, **74**:231-249, 1981

Scott, K. P., K. J. Thome, and M. R. Brownlee, "Evaluation of the Railroad Valley playa for use in vicarious calibration," *Proc. SPIE Conf. #2818*, Denver, Colorado, 1996.

Sicard, M., K. J. Thome, B. G. Crowther, and M. W. Smith, "Shortwave infrared spectroradiometer for atmospheric transmittance measurements," submitted to *J. of Atmos. and Oceanic Tech.*, 1997.

Slater, P. N, S. F. Biggar, K. J. Thome, D. I. Gellman, and P. R. Spyak, "Vicarious radiometric calibrations of EOS Sensors," *J. of Atmos. and Oceanic Tech..*, **13**:349-359, 1996.

Slater, P. N, S. F. Biggar, R. G. Holm, R. D. Jackson, Y. Mao, M. S. Moran, J. M. Palmer, and B. Yuan, "Reflectance- and radiance-based methods for the in-flight absolute calibration of multispectral sensors," *Rem. Sens. Env.*, **22**:11-37, 1987.

Smith, J., K. Thome, B. Crowther, S. Biggar, "Field evaluation of a diffuse-to-global irradiance meter for vicarious calibration," *International Geoscience and Remote Sensing Symposium*, Seattle, Washington, pp. 562-564, 1998.

Spyak, P. R. and C. Lansard, "Reflectance properties of pressed Algoflon F6: a replacement reflectance-standard material for Halon," *Appl. Opt.*, **36**:2963-2970, 1997.

Teillet, P. M., P. N. Slater, Y. Ding, R. P. Santer, R. D. Jackson, and M. S. Moran, "Three methods for the absolute calibration of the NOAA AVHRR sensors in-flight," *Rem. Sens. Env.*, **31**:105-120, 1990.

Teillet, P. M., "An algorithm for the radiometric and atmospheric correction of AVHRR data in the solar reflective," *Rem. Sens. Env.*, **41**:185-195, 1992.

Thome, K. J., B.M. Herman, and J.A. Reagan, "Determination of precipitable water from solar transmission," *J. of Appl. Met.*, **31**:157-165, 1992.

Thome, K. J., C. L. Gustafson-Bold, P. N. Slater, and W. H. Farrand. "In-flight radiometric calibration of HYDICE using a reflectance-based approach," *Proc. SPIE Conf. 2821*, Denver, Colorado, 1966.

Thome, K. J., M. W. Smith, J. M. Palmer, and J. A. Reagan, "Three-channel solar radiometer for determining atmospheric columnar water vapor," *Appl. Optics*, **33:**5811-5819, 1994.

Thuillier, G., M. Herse, P. C. Simon, D. Labs, H. Mandel, G. Gillotay, and T. Foulols, "The visible solar spectral irradiance from 350 to 850 nm as measured by the SOLSPIC spectrometer during the ATLAS-1 mission," in press *Solar Physics*, 1997.

Zalewski, E. F. and C. R. Duda, "Silicon photodiode device with 100% external quantum efficiency," *Applied Optics*, **22**:2867, 1983.

APPENDICES

Appendix A - Acronyms and Abbreviations

ASTER	Advanced Spaceborne Thermal and Emissivity and Reflection Radiometer
AVHRR	Advanced Very High Resolution Radiometer
AVIRIS	Airborne Visible and Infrared Imaging Spectrometer
BRDF	Bi-directional reflectance distribution function
BRF	Bi-directional reflectance factor
CCR	Cross-calibration radiometer
DAAC	Data Active Archive Center
DN	Digital Number
EOS	Earth Observing System
ESE	Earth Science Enterprise
ETM+	Enhanced Thematic Mapper+
FOV	Field of view
HRF	Hemispherical-directional reflectance factor
HRV	Haute Resolute Visible
JAC	Japanese ASTER Calibration
JPL	Jet Propulsion Laboratory
MAS	MODIS Airborne Simulator
MASTER	MODIS/ASTER Airborne Simulator
MCST	MODIS Calibration Support Team
MISR	Multi-angle Imaging Spectroradiometer
MODIS	MODerate Resolution Imaging Spectroradiometer
NIST	National Institute of Standards and Technology
NLAPS	National Landsat Archive Production System
ORNL	Oak Ridge National Laboratory
RSG	Remote Sensing Group
RTC	Radiative transfer code
SeaWiFS	Sea-viewing Wide Field of View Sensor
SDSU	South Dakota State Universtiy
SIS	Spherical Integrating Source
SPOT	Syteme Pour l'Observation del la Terra
SWIR	Shortwave infrared
TIR	Thermal infrared
TM	Thematic Mapper
TOA	Top of the atmosphere
VC	Vicarious Calibration
VNIR	Visible and near-infrared